TRADE STUDIES FOR THE GBM TRIGGER

David Band

1.   Introduction

To assist the design effort for the GBM burst trigger, I am undertaking a number of trade studies. This memo describes the results; it will evolve as I add additional studies. Currently the memo addresses time binning and the choice of the trigger energy bands ΔE.

The underlying assumption is that the GBM will use a rate trigger: a detector will trigger when the number of counts in a time bin of duration Δt and in an apparent energy range ΔE exceeds the expected number of background counts by a preset number of multiples of the fluctuation scale, the square root of the number of expected background counts. For the array of NaI detectors a trigger occurs when the significance in two or more detectors exceeds a threshold, here assumed to be $\sigma_0 = 5.5$. For the BGO detectors I assume a significance in one detector of $\sigma_0 = 8$ is required.

2.   Time Binning

The time binning issues are what values of Δt should be used, and what registration of consecutive time bins should be used.

BATSE used Δt=64 ms, 256 ms, and 1024 ms, i.e., Δt spaced by factors of $\times 4$. We realize that both shorter and longer values of Δt would have probed different burst populations at the detection threshold. The GBM can use a minimum time of Δt=16 ms, and we would like to try Δt up to ~ 16 s. The question is whether the values of Δt should be spaced by factors of $\times 2$ (i.e., Δt=16 ms, 32 ms, 64 ms...) or of $\times 4$ (i.e., Δt=16 ms, 64 ms, 256 ms...).

BATSE used time bins that did not overlap. Thus the Δt=1024 ms bins were accumulated every 1024 ms. A burst would have triggered BATSE at a lower peak flux if the peak fell mostly in one 1024 ms bin than if the peak was split between two bins. The opposite extreme would be to use every possible time bin; thus the GBM would test bins staggered by only 16 ms. This would involve a great deal of computation, and would most likely not gain much sensitivity for larger values of Δt. The probability of a large fluctuation increases as the number of bins tested increases, but the increase is not linear because the bins are not independent. An improvement on the non-overlapping time bins would be to accumulate

bins (beyond the shortest Δt) every $\Delta t/2$. Thus the Δt=1024 ms bins would be accumulated every 512 ms.

I tested 6 different triggers: two Δt spacings, and three time bin registrations. I label the non-overlapping bins "FULL" (for full step), bins every half step "HALF," and all possible bins "ALL." I append a 2 or 4 if Δt is spaced by $\times 2$ or $\times 4$. Thus the most tests will occur for ALL2, and the least for FULL4. Over 16.384 s with Δt between 16 ms and 16.384 s, 11264 time bins will be tested for ALL2, but only 6144 for ALL4. FULL2 results in 2047 bins, and 1365 bins for FULL4. HALF2 results in 3070 bins and HALF4 in 1706. Note that the computation time may not scale linearly with the number of bins tested; for the trigger algorithm I developed, the counts-in-a-bin are calculated for Δt spaced by factors of $\times 2$ whether or not a particular Δt is tested.

To test the sensitivity of these 6 different triggers, I applied each trigger to the 50–300 keV lightcurves with 64 ms resolution of the 25 BATSE bursts (for which there are data) with the largest peak fluxes integrated over 64 ms. In each case I chose 10 different starting times randomly distributed over 16.384 s, thus sampling different registrations of the burst relative to the grid of time bins. If the jth bin has C_j counts where B_j are expected, the trigger significance for that bin is $(C_j - B_j)/\sqrt{B_j}$. The maximum trigger significance for a burst is proportional to how much fainter the burst could have been and still would have been detected. Ratios of the maximum significances for different triggers compares the relative sensitivities of these triggers. I have chosen to calculate ratios that are greater than or equal to 1, thus showing the factor by which peak flux threshold for the less sensitive trigger is greater than for the more sensitive trigger. The figure shows the cumulative distribution of these ratios—there are 250 samples (25 bursts with 10 beginning times for each burst). As can be seen, HALF2 is the most sensitive trigger after ALL2, while FULL4 is the least sensitive trigger, as expected. As a quantitative measure of the sensitivities of the different triggers, I consider the relative sensitivity at 0.1, i.e., for 10% of the cases the relative sensitivity will be greater than this value: ALL4—1.147; HALF2—1.108; HALF4—1.236; FULL2—1.271; and FULL4—1.345. HALF2 may be a particularly effective trigger.

While testing more time bins increases the detection sensitivity, it also increases the probability of a spurious trigger. If more time bins are tested and the overall probability of a spurious trigger is to remain the same, then the trigger threshold needs to be set higher, reducing the detection sensitivity. Since overlapping bins are tested by many of these triggers, the probability of a spurious trigger is not proportional to the number of bins; the bins are not independent. Thus the question is whether the increase in sensitivity for more bins is balanced by the greater probability of a spurious trigger.
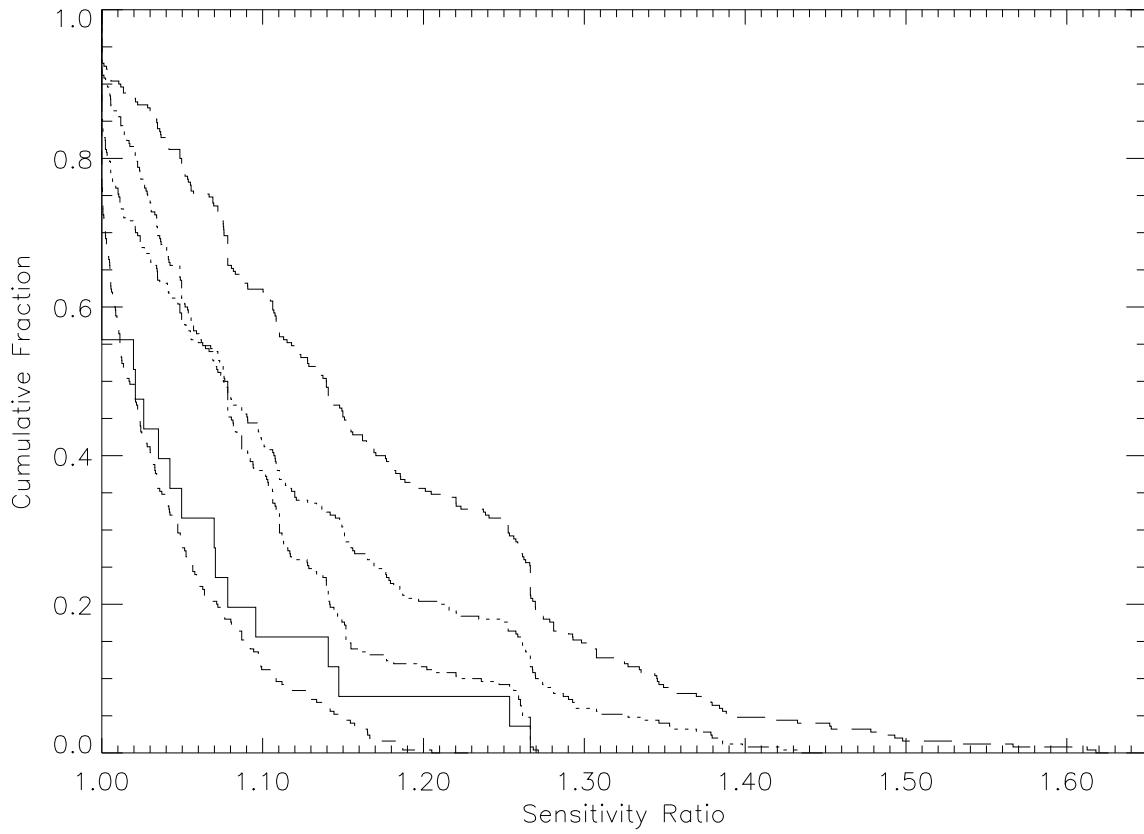
Fig. 1.— Cumulative distribution of the sensitivity for different triggers relative to ALL2, the most sensitive trigger. The curves are: solid—ALL4; dashed—HALF2; dot-dashed—HALF4; dots-dashed—FULL2; and long dashed—FULL4. The results are for 25 strong BATSE bursts, each with 10 different beginning times.

To determine the spurious trigger rate for the different triggers, I ran the triggers over 640 s (10,000 bins of 0.064 s each) of simulated background. The number of counts in each bin was drawn from a Poisson distribution with a specified mean equal to the background rate. For each interval I recorded the maximum significance for each trigger on any timescale; since there was not bursts in these simulations, this significance results from a fluctuation. Figures 2–5 show the cumulative distribution for 1000 intervals for background rates of 250 and 1000 counts per 64 ms bin. As can be seen, the more sensitive triggers do have higher maximum significances for simulated background. For the same fluctuation probability the threshold significance needs to be raised by less than $\sim 5\%$.

3.   Dependence of Sensitivity on E_p

Marc Kippen has provided his code that calculates the total and background counts accumulated in each detector over a specified energy band ΔE and time range Δt for a burst with a given spectrum and position relative to the spacecraft. Thus for the ith detector, the code provides C_i total and B_i background counts over Δt between E_1 and E_2 for a burst photon flux N_B. For the GRB spectral shape the normalization n_K is the photon flux integrated between 50 and 300 keV. The significance is

$$\sigma = \frac{\Delta t \int_{E_1}^{E_2} dE' R_i(E'|E,\Omega)N_B(E)}{\sqrt{B_i}} = \frac{C_i - B_i}{\sqrt{B_i}} \tag{1}$$

where $R_i(E'|E,\Omega)$ is the response function linking the count rate in the ith detector at an apparent energy E' with the actual photon energy E from a source at location Ω.

I advocate using the threshold peak flux F_T integrated between 1 and 1000 keV as the sensitivity. The corresponding photon flux is $N_T = mN_B$; the spectral shape is the same, but the fluxes differ by a normalizing factor. Assume that a trigger significance of σ_0 is required. Then

$$F_T = \int_1^{1000} dE N_T(E) \quad , \tag{2}$$

$$\sigma_0 = \frac{\Delta t \int_{E_1}^{E_2} dE' R_i(E'|E,\Omega)N_T(E)}{\sqrt{B_i}} \quad , \tag{3}$$

$$\text{and therefore } F_T = \frac{\int_1^{1000} dE N_T(E) \times \sigma_0 \sqrt{B_i}}{\Delta t \int_{E_1}^{E_2} dE' R_i(E'|E,\Omega)N_T(E)} \quad , \tag{4}$$

where I have multiplied eqn. (2) by the left side of eqn. (3) divided by the right side (i.e.,
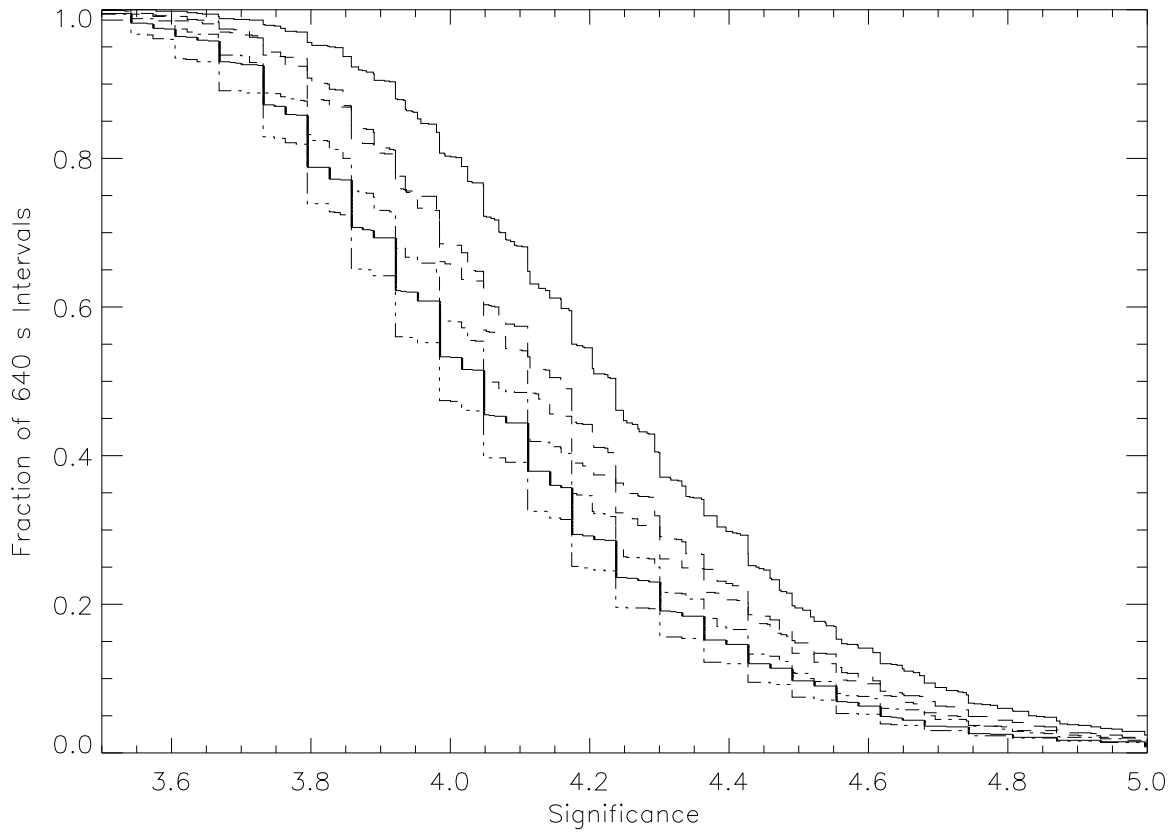
Fig. 2.— Cumulative distribution of maximum significance in a 640 s interval of simulated background. The background rate was 250 counts per 64 ms bin, and 1000 intervals were run. The curves are: upper solid curve—ALL2; dashed—ALL4; dot-dashed—FULL2; dots-dashed—FULL4; long-dashed—HALF2; and lower solid curve—HALF4.
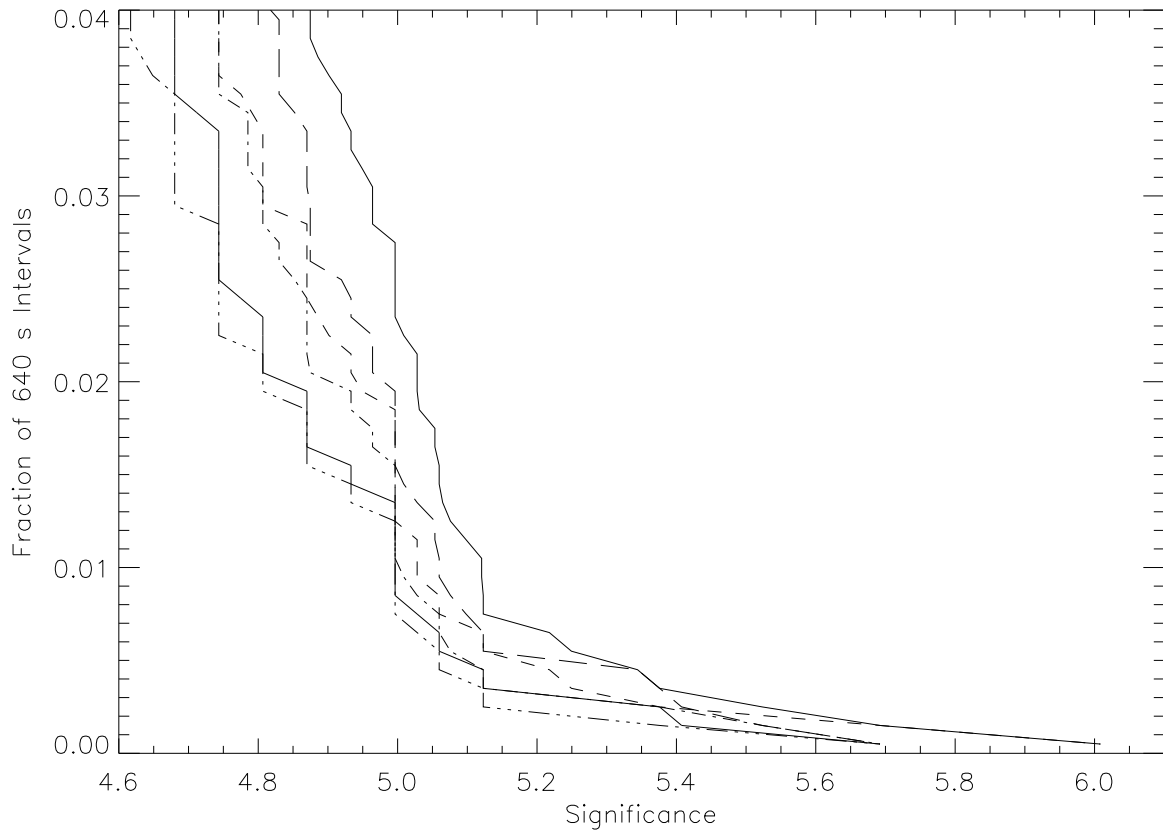
Fig. 3.— Same as Figure 2 (background rate of 250 counts per 64 ms bin), but showing the high significance tail.
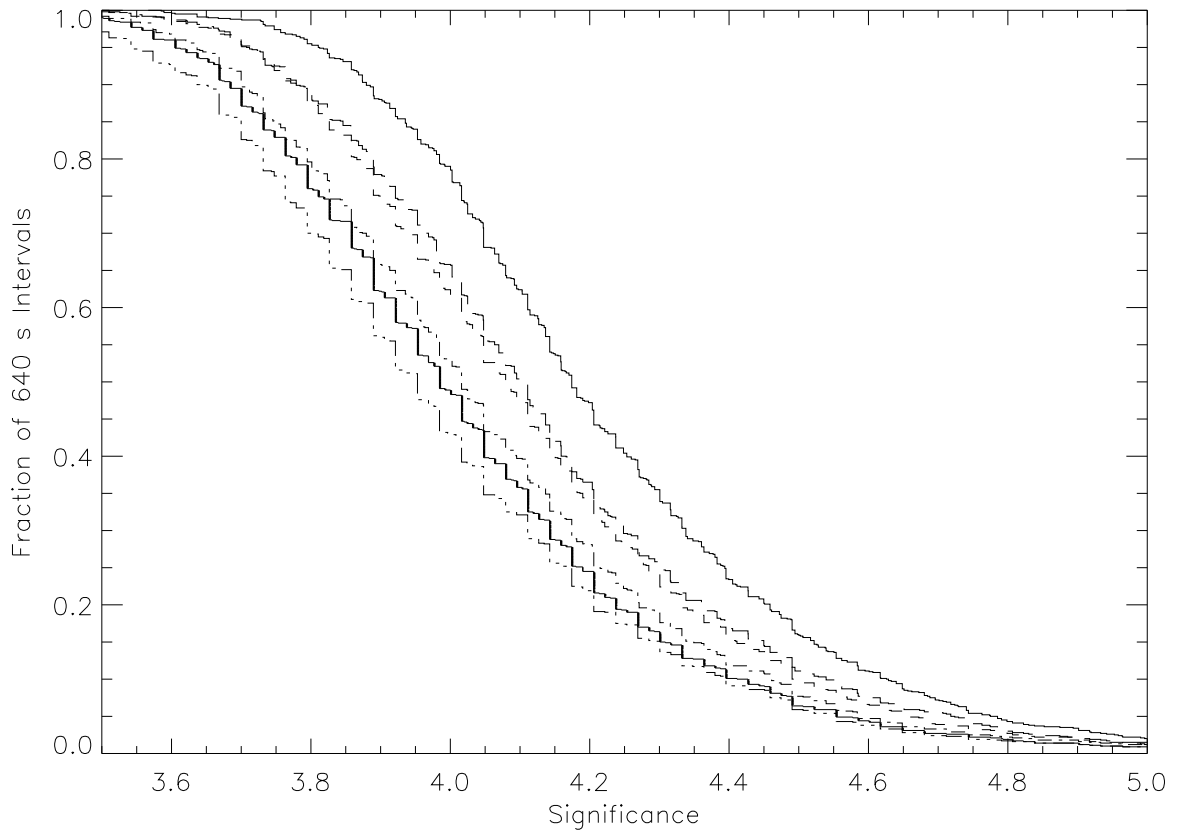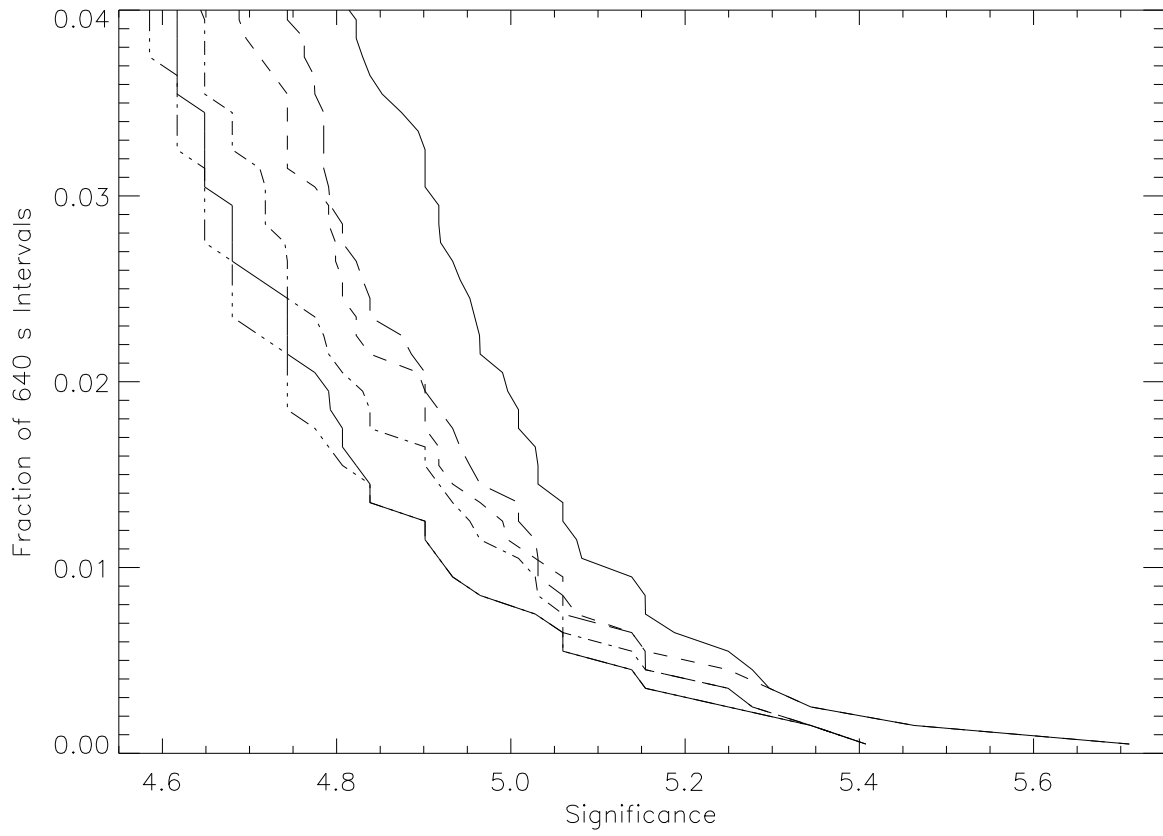
Fig. 4.— Same as Figure 2, but for 1000 counts per 64 ms bin.

Fig. 5.— Same as Figure 4 (background rate of 1000 counts per 64 ms bin), but showing the high significance tail.

by 1). But since

$$C_i - B_i = \Delta t \int_{E_1}^{E_2} dE' R_i(E'|E,\Omega) N_B(E) \quad, \tag{5}$$

$$\text{then } F_T = \frac{\int_1^{1000} dE N_T(E) \times \sigma_0 \sqrt{B_i}}{m(C_i - B_i)} \quad, \tag{6}$$

where m is the ratio between N_T and N_B. In deriving eqn. (6) I used the numerators in eqn. (1) and the scaling between N_T and N_B. But since

$$\int_{50}^{300} dE N_T(E) = m \int_{50}^{300} dE N_B(E) = m n_K \quad, \tag{7}$$

$$\text{therefore } F_T = \left[\frac{n_k \int_1^{1000} dE N_T(E)}{\int_{50}^{300} dE N_T(E)} \right] \left[\frac{\sigma_0 \sqrt{B_i}}{C_i - B_i} \right] \quad . \tag{8}$$

Note that integrals over N_T are in both the numerator and denominator, and thus the actual normalization of N_T is never calculated. The shape of the spectrum is necessary for both N_T and the calculation of C_i; I parameterize the burst spectrum with the GRB function. The source direction affects the calculation of C_i; the detector with the second largest value of C_i (resulting in the second largest value of σ) should be chosen.

First I evaluate the spatial sensitivity of the GBM NaI array; eventually this should be done more systematically. Figures 6 and 7 show the sensitivity as a function of zenith and azimuth. As can be seen the sensitivity varies away from the normal to the LAT, but within the LAT's FOV the variations are $\sim 20\%$.

Next I considered the choice of ΔE—the energy bands over which the counts will accumulated. The channel boundaries can be: 5, 10, 20, 50, 100, 300, 500, 1000 and > 1000 keV. For these studies I've avoided the highest boundary since it is not well defined. To compare GBM results with BATSE we would like to use $\Delta E = 50$–300 keV. I use four sets of spectral indices: $\alpha = -1$, $\beta = -2$; $\alpha = -1/2$, $\beta = -3$; $\alpha = 0$, $\beta = -2$; and $\alpha = -1$, $\beta = -25$. To get significant flux in the LAT even for strong bursts, the spectrum should be hard ($E_p \sim 1$ MeV) with $\beta \sim -2$. Bursts are often hard at the beginning of bursts with $\alpha \sim 0$; thus the third set of spectral indices is particularly interesting. The fourth set corresponds to a spectrum with no high energy tail.

In general I find that starting ΔE at 5 keV or ending at 1000 keV maximizes the sensitivity. For example $\Delta E = 5$–100 keV is generally more sensitive than $\Delta E = 10$–100 keV. Starting at a given low energy boundary, the trigger is more sensitive for a higher high energy boundary; for example $\Delta E = 5$–100 keV is more sensitive than $\Delta E = 5$–50 keV. Figures 8–11 show the curves for ΔE ending at 1000 keV. Starting the energy band at 5 keV provides the
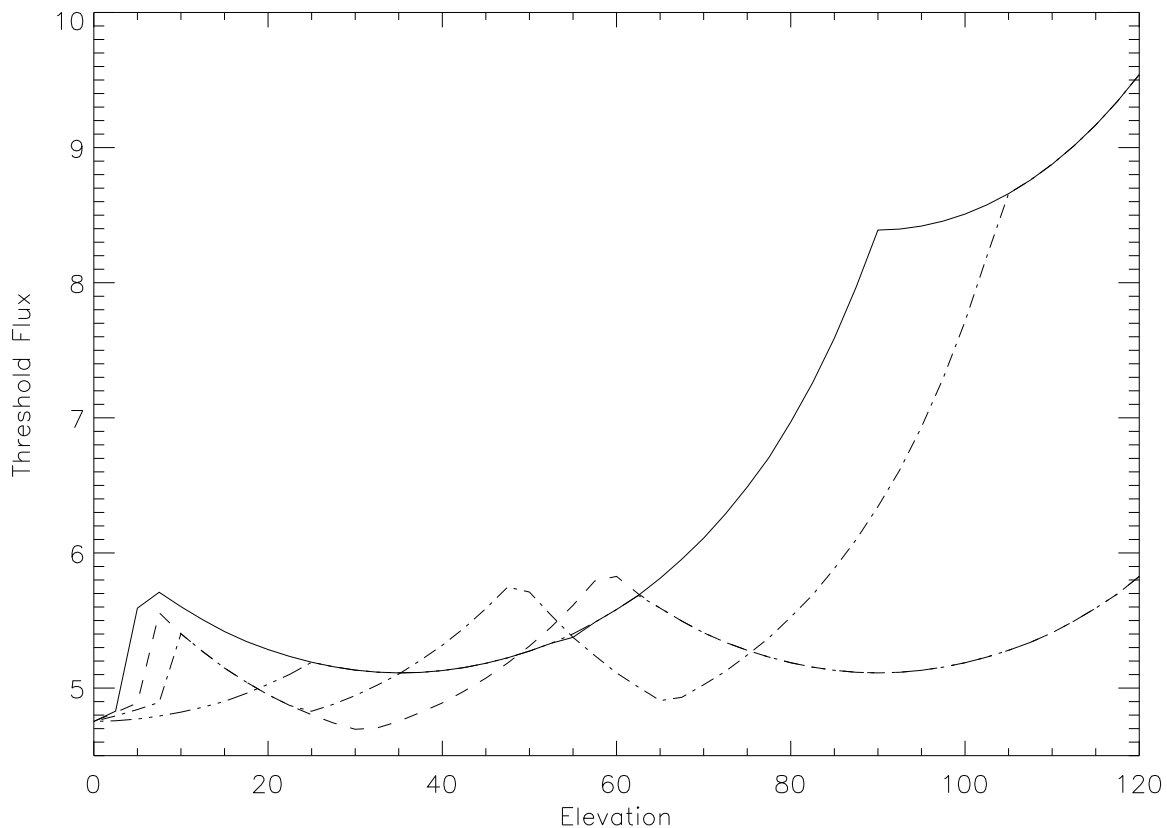
Fig. 6.— The sensitivity of the GBM NaI array as a function of zenith (here labelled as elevation) angle (angle from the normal to the LAT). The curves are for different azimuth angles: solid—0°; dashed—30°; dot-dashed—60°; and dots-dashed—90°. The spectral model is $\alpha = -1$, $\beta = -2$, and $E = 100$ keV; $\sigma_0 = 5.5$ is assumed. The calculation is for $\Delta E = 10$–100 keV and 50–300 keV, and $\Delta t = 1$ s. The threshold flux is the 1–1000 keV peak flux (ph s^{-1} cm^{-2}).
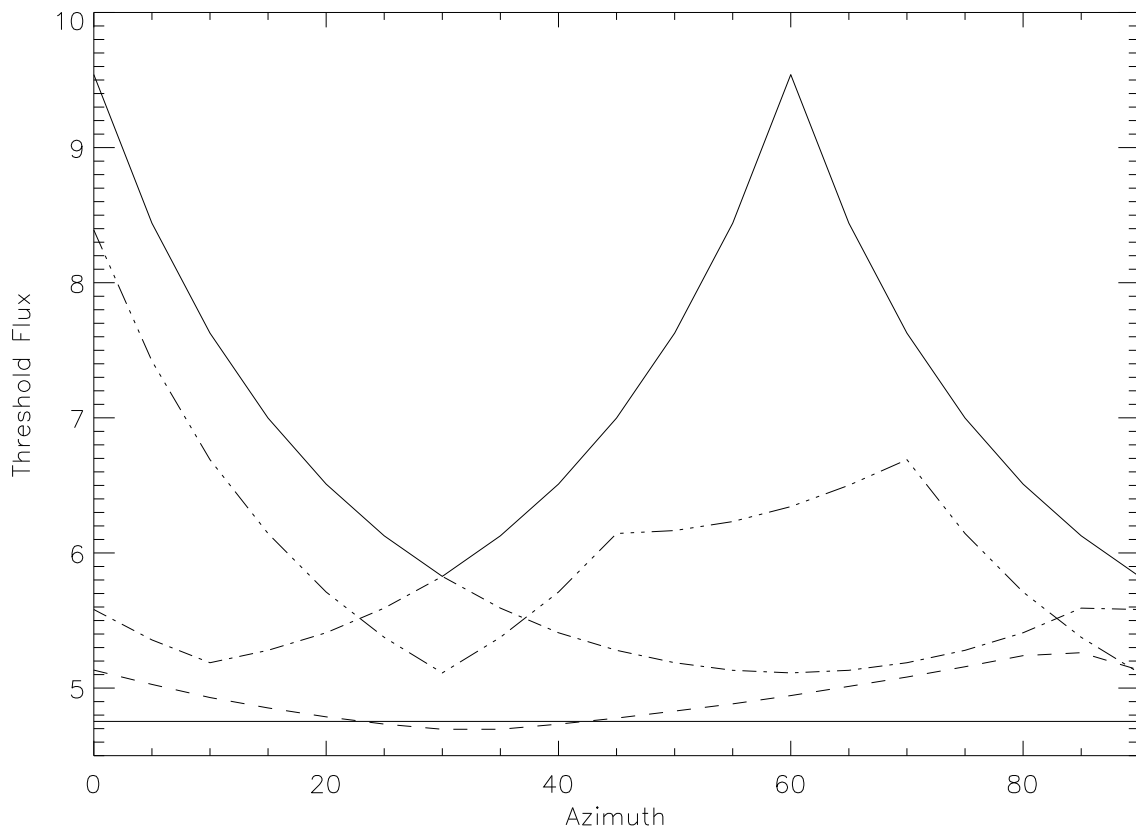
Fig. 7.— The sensitivity of the GBM NaI array as a function of azimuth angle; because of the symmetry, only azimuths between 0° and 90° are shown. The curves are for different zenith angles: lower solid—0°; dashed—30°; dot-dashed—60°; dot-dot-dashed—90°; and upper solid—120°. The spectral model is $\alpha = -1$, $\beta = -2$, and $E = 100$ keV; $\sigma_0 = 5.5$ is assumed. The calculation is for $\Delta E = 10$–100 keV and 50–300 keV, and $\Delta t = 1$ s. The threshold flux is the 1–1000 keV peak flux (ph s^{-1} cm^{-2}).

best low energy sensitivity, while starting at 50 or 100 keV provides the best high energy sensitivity, although the results vary with spectral index. Ending ΔE at 300 keV has a similar pattern. Figures 12–15 show the sensitivity curves for ΔE beginning at 5 keV. As can be seen, including the entire energy band gives the greatest sensitivity in all cases.

Based on these results I advocate using ΔE=5–100, 50–300, and 100–1000 keV. This may not be the optimum, but it includes ΔE=50–300 keV. Alternatively ΔE=5–1000 keV may be used instead of 5–100 keV, and 100–>1000 can be used instead of 100-1000 keV. If we do not require ΔE=50–300 keV, then ΔE=5–1000 and 50–1000 keV would do a good job. Figures 16–19 compare two sets of ΔE for the different sets of spectral indices.

4. Triggering Off the BGO Detectors

Will triggering off the BGO detectors increase the GBM sensitivity? To answer this question I assume the GBM will trigger off a single detector (as opposed to requiring two NaI detectors trigger), but raise the trigger threshold to $\sigma_0 = 8$. I use two BGO trigger bands: ΔE=0.15–1 MeV and 0.15–30 MeV. For comparison I include the sensitivity resulting from triggering off two NaI detectors with ΔE=5–1000 keV and 50–300 keV. Figures 20–22 show the results for: $\alpha = 0$, $\beta = -2$; $\alpha = -1$, $\beta = -2$; and $\alpha = -1$, $\beta = -5$. As can be seen, the BGO provides extra sensitivity only for $\alpha = 0$, $\beta = -2$ above E_p=1 MeV. As I argued above, the spectrum at the beginning of a burst often has $\alpha = 0$, $\beta = -2$, and therefore the BGO trigger will provide extra sensitivity to hard bursts that might have significant LAT flux.
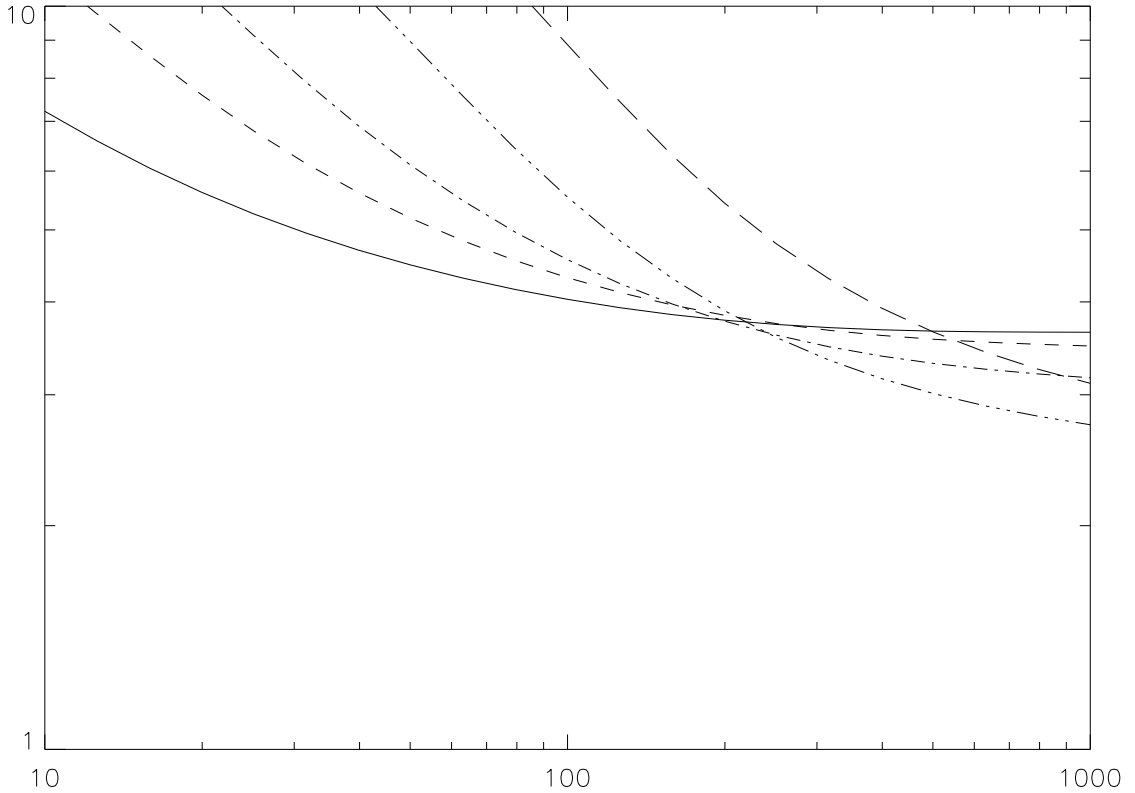
Fig. 8.— The sensitivity of the GBM NaI array as a function of ΔE for $\alpha = -1$ and $\beta = -2$. For all curves ΔE ends at 1000 keV. The lower end is at 5 (solid curve), 10 (dashes), 20 (dot-dashes), 50 (dots-dashes) and 100 keV (long dashes). The calculation is $\sigma_0 = 5.5$ and a zenith angle of 0°. The y-axis is the 1–1000 keV peak flux (ph s^{-1} cm^{-2}), while the x-axis is E_p in keV.
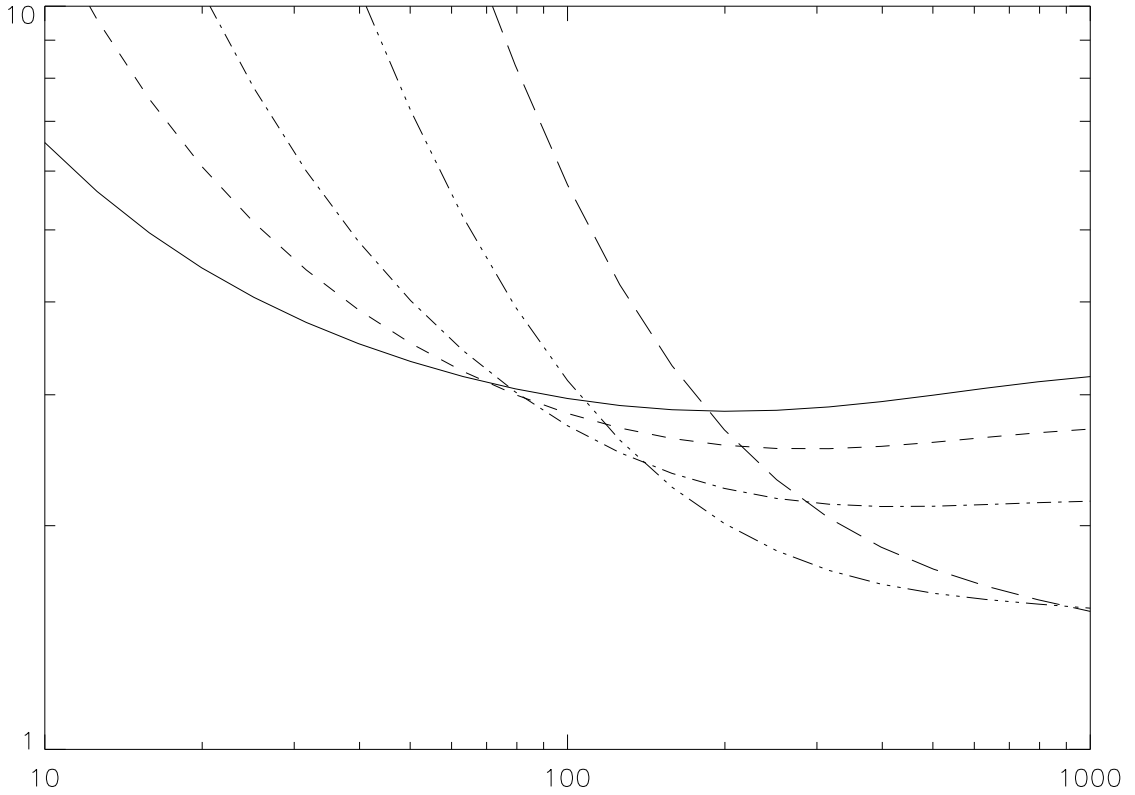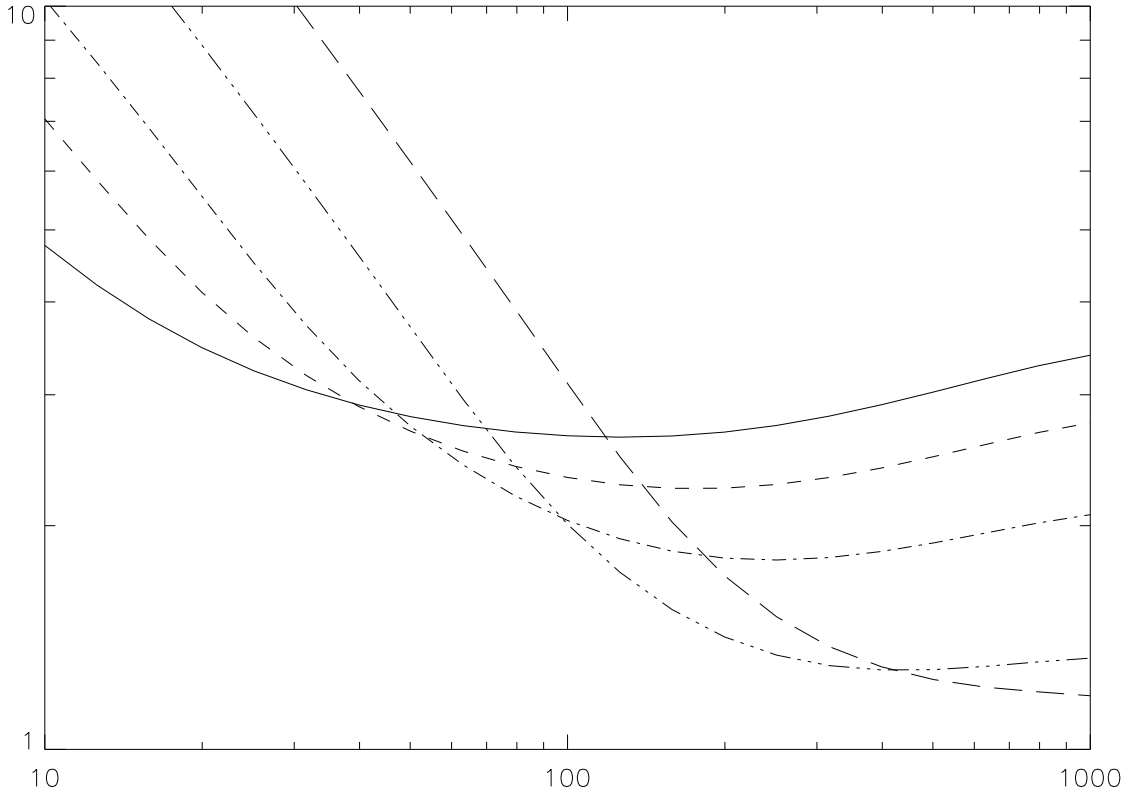
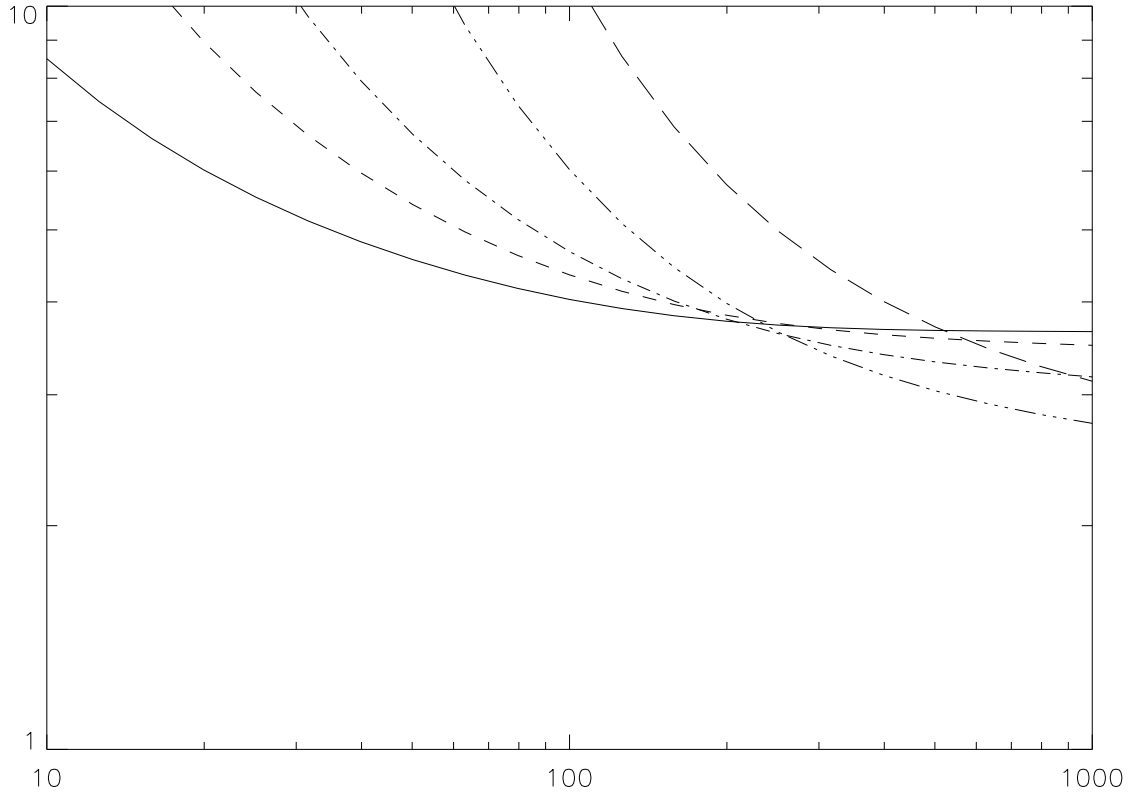Fig. 9.— The sensitivity of the GBM NaI array as a function of ΔE for $\alpha = -1/2$ and $\beta = -3$. For all curves ΔE ends at 1000 keV. The lower end is at 5 (solid curve), 10 (dashes), 20 (dot-dashes), 50 (dots-dashes) and 100 keV (long dashes). The calculation is $\sigma_0 = 5.5$ and a zenith angle of $0°$. The y-axis is the 1–1000 keV peak flux (ph s^{-1} cm^{-2}), while the x-axis is E_p in keV.

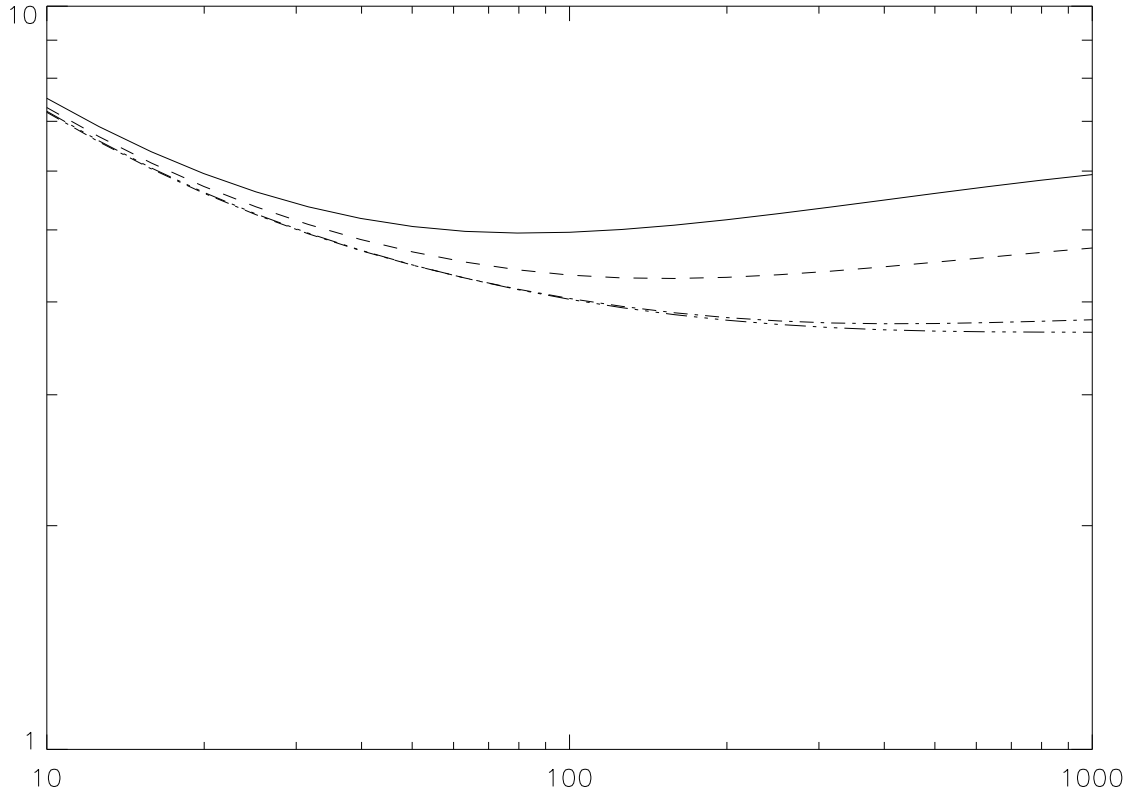Fig. 10.— The sensitivity of the GBM NaI array as a function of ΔE for $\alpha = 0$ and $\beta = -2$. For all curves ΔE ends at 1000 keV. The lower end is at 5 (solid curve), 10 (dashes), 20 (dot-dashes), 50 (dots-dashes) and 100 keV (long dashes). The calculation is $\sigma_0 = 5.5$ and a zenith angle of 0°. The y-axis is the 1–1000 keV peak flux (ph s^{-1} cm^{-2}), while the x-axis is E_p in keV.

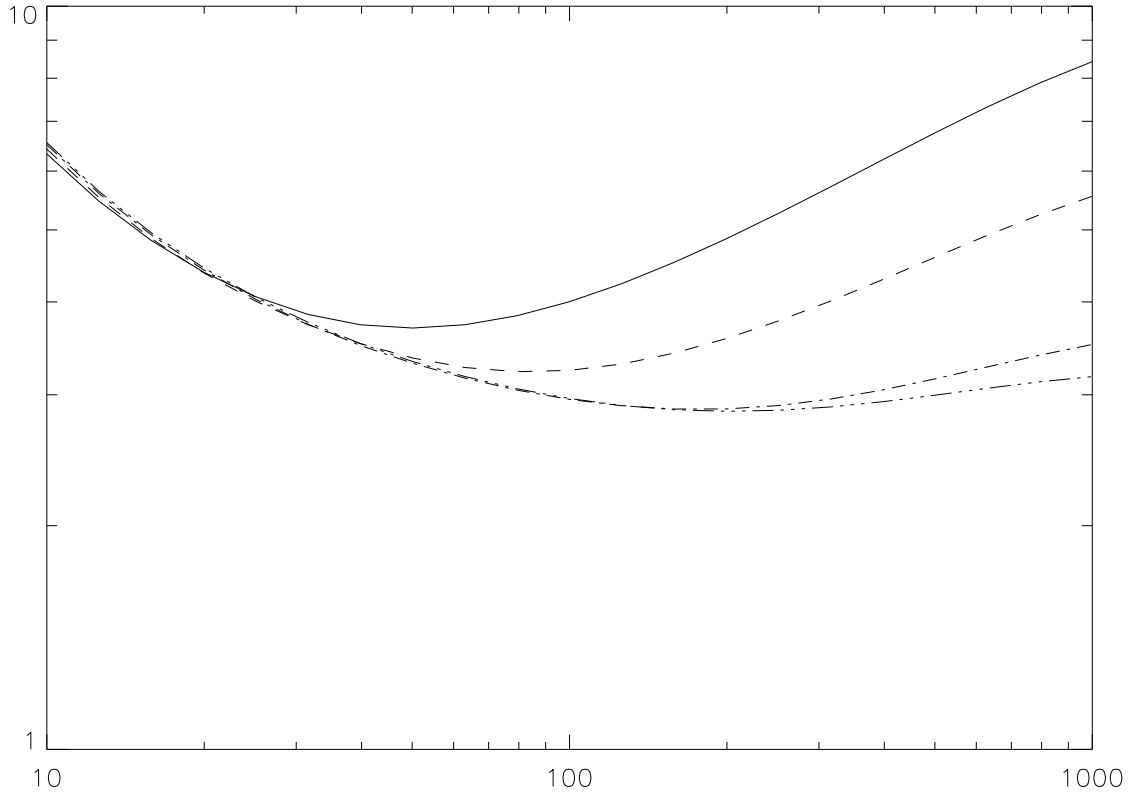Fig. 11.— The sensitivity of the GBM NaI array as a function of ΔE for $\alpha = -1$ and $\beta = -25$. For all curves ΔE ends at 1000 keV. The lower end is at 5 (solid curve), 10 (dashes), 20 (dot-dashes), 50 (dots-dashes) and 100 keV (long dashes). The calculation is $\sigma_0 = 5.5$ and a zenith angle of $0°$. The y-axis is the 1–1000 keV peak flux (ph s^{-1} cm^{-2}), while the x-axis is E_p in keV.

Fig. 12.— The sensitivity of the GBM NaI array as a function of ΔE for $\alpha = -1$ and $\beta = -2$. For all curves ΔE begins at 5 keV. The upper end is at 50 (solid curve), 100 (dashes), 300 (dot-dashes), and 1000 keV (dots-dashes). The calculation is $\sigma_0 = 5.5$ and a zenith angle of $0°$. The y-axis is the 1–1000 keV peak flux (ph s^{-1} cm^{-2}), while the x-axis is E_p in keV.
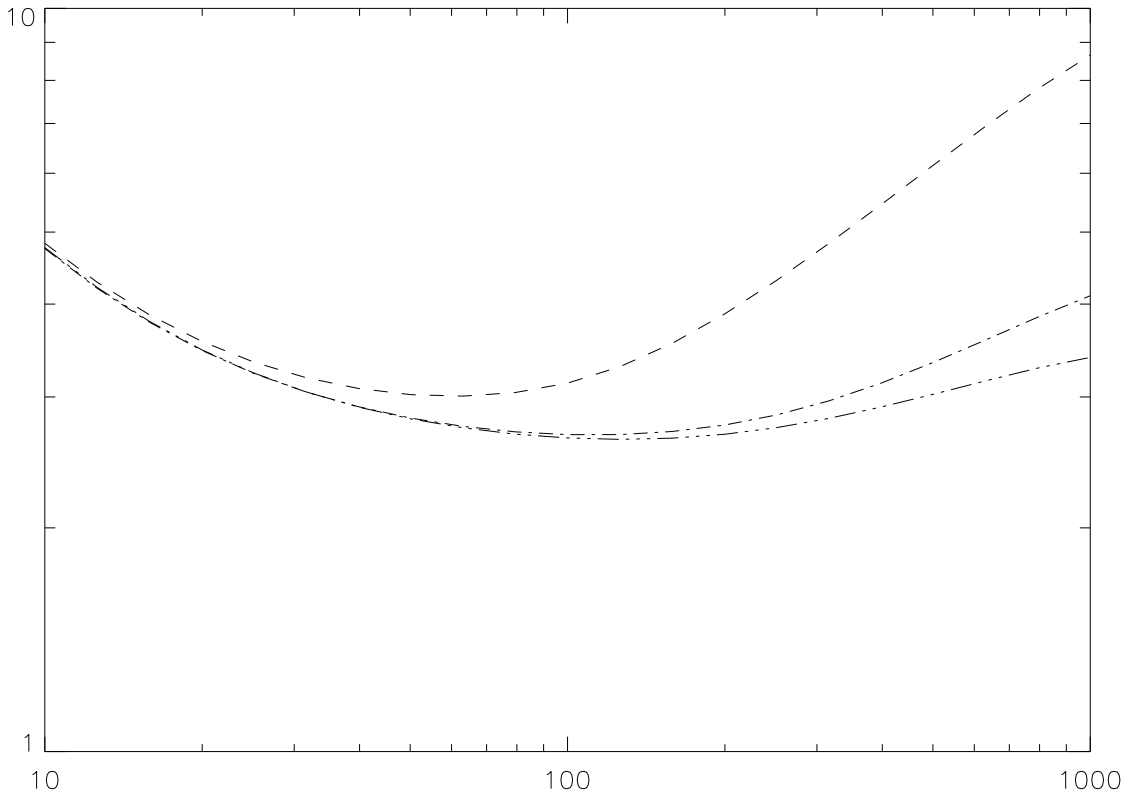
Fig. 13.— The sensitivity of the GBM NaI array as a function of ΔE for $\alpha = -1/2$ and $\beta = -3$. For all curves ΔE begins at 5 keV. The upper end is at 50 (solid curve), 100 (dashes), 300 (dot-dashes), and 1000 keV (dots-dashes). The calculation is $\sigma_0 = 5.5$ and a zenith angle of $0°$. The y-axis is the 1–1000 keV peak flux (ph s^{-1} cm^{-2}), while the x-axis is E_p in keV.
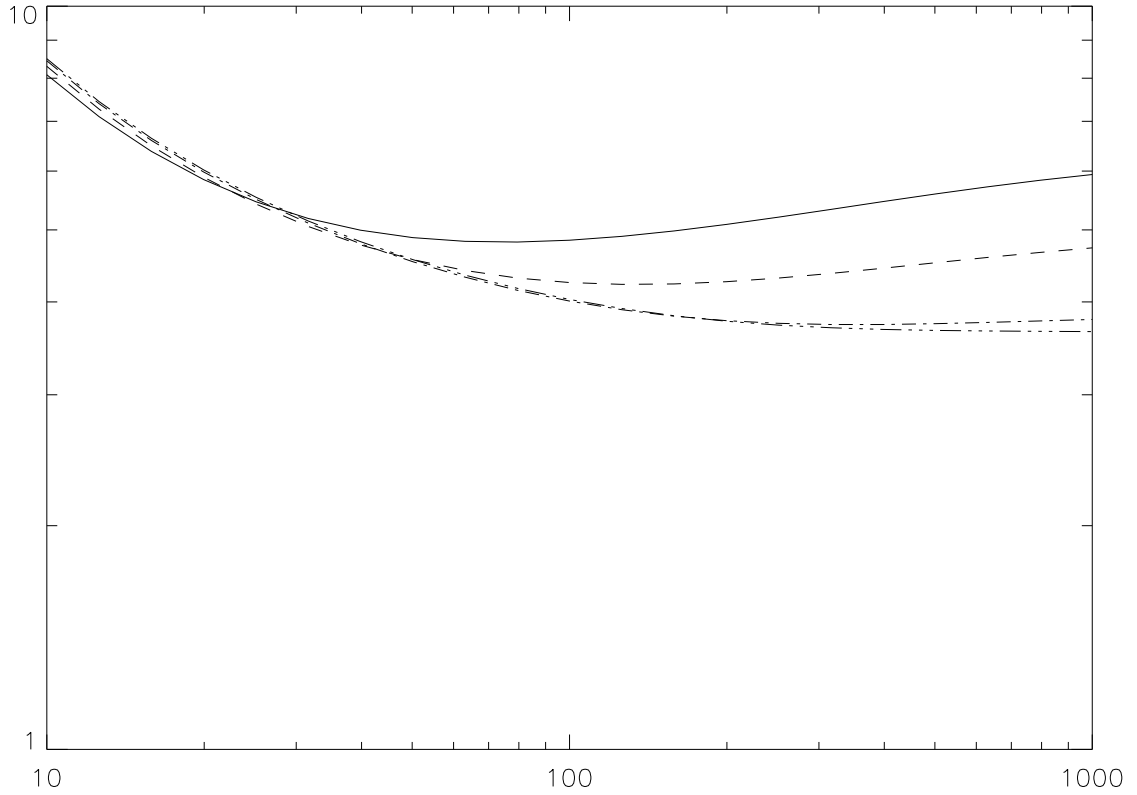
Fig. 14.— The sensitivity of the GBM NaI array as a function of ΔE for $\alpha = 0$ and $\beta = -2$. For all curves ΔE begins at 5 keV. The upper end is at 50 (solid curve), 100 (dashes), 300 (dot-dashes), and 1000 keV (dots-dashes). The calculation is $\sigma_0 = 5.5$ and a zenith angle of $0°$. The y-axis is the 1–1000 keV peak flux (ph s^{-1} cm^{-2}), while the x-axis is E_p in keV.
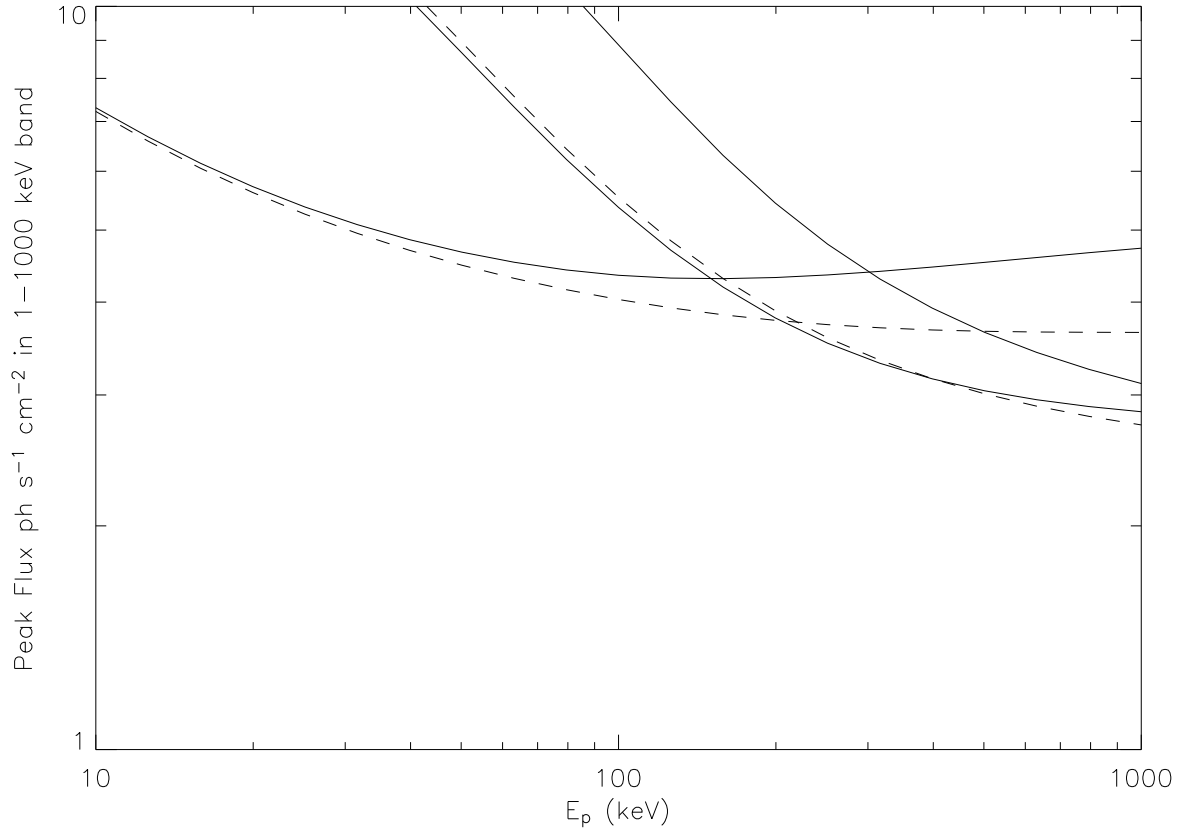
Fig. 15.— The sensitivity of the GBM NaI array as a function of ΔE for $\alpha = -1$ and $\beta = -25$. For all curves ΔE begins at 5 keV. The upper end is at 50 (solid curve), 100 (dashes), 300 (dot-dashes), and 1000 keV (dots-dashes). The calculation is $\sigma_0 = 5.5$ and a zenith angle of 0°. The y-axis is the 1–1000 keV peak flux (ph s^{-1} cm^{-2}), while the x-axis is E_p in keV.
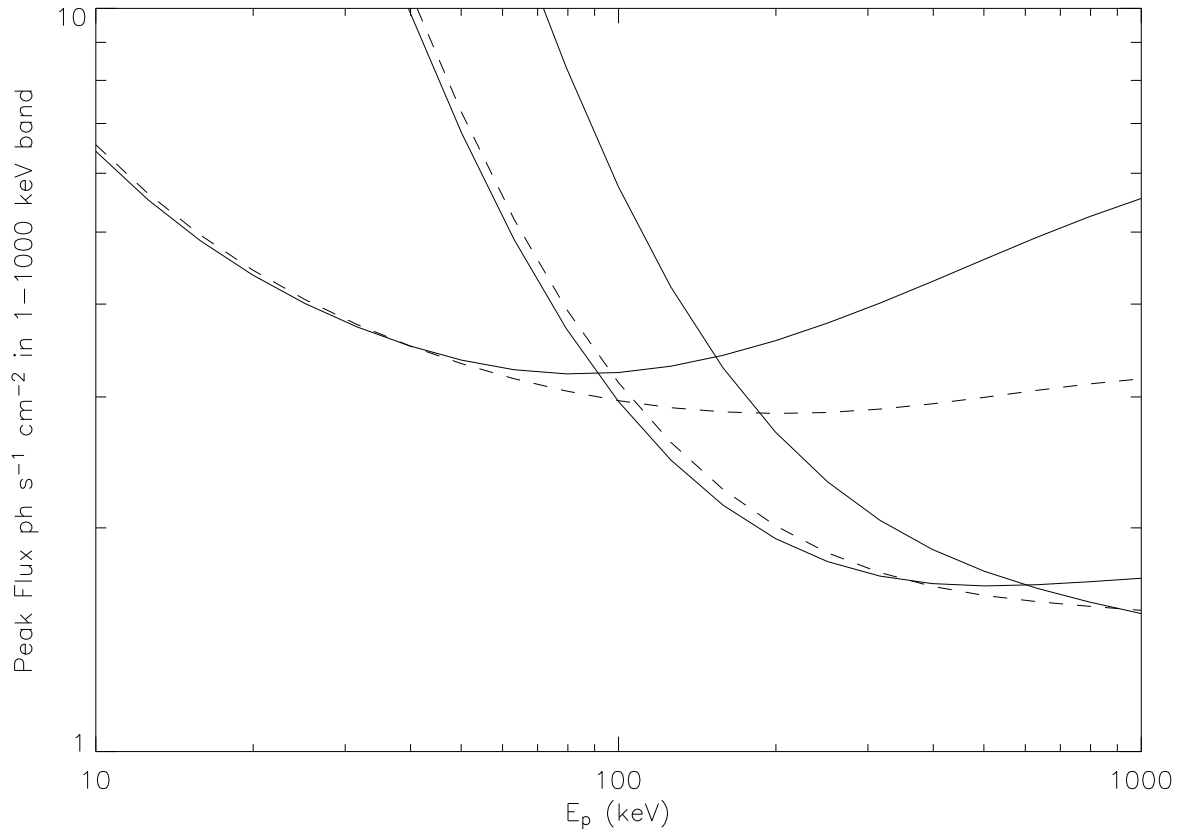
Fig. 16.— Two sets of ΔE for $\alpha = -1$ and $\beta = -2$. For the first (solid curves) ΔE=5–100, 50–300, and 100–1000 keV while for the second (dashed curves) ΔE=5–1000 and 50—1000 keV. The calculation is $\sigma_0 = 5.5$ and a zenith angle of 0°. The y-axis is the 1–1000 keV peak flux (ph s^{-1} cm^{-2}), while the x-axis is E_p in keV.

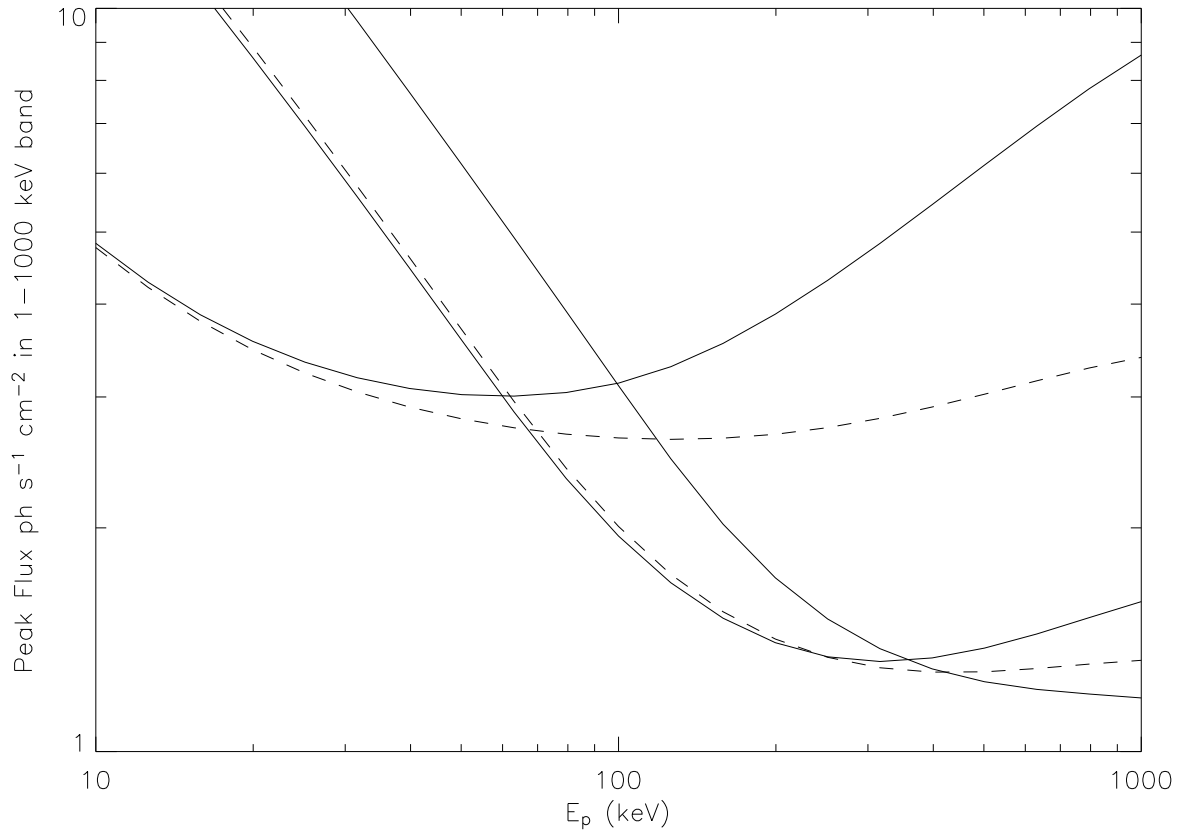Fig. 17.— Two sets of ΔE for $\alpha = -1/2$ and $\beta = -3$. For the first (solid curves) ΔE=5–100, 50–300, and 100–1000 keV while for the second (dashed curves) ΔE=5–1000 and 50—1000 keV. The calculation is $\sigma_0 = 5.5$ and a zenith angle of 0°. The y-axis is the 1–1000 keV peak flux (ph s^{-1} cm^{-2}), while the x-axis is E_p in keV.

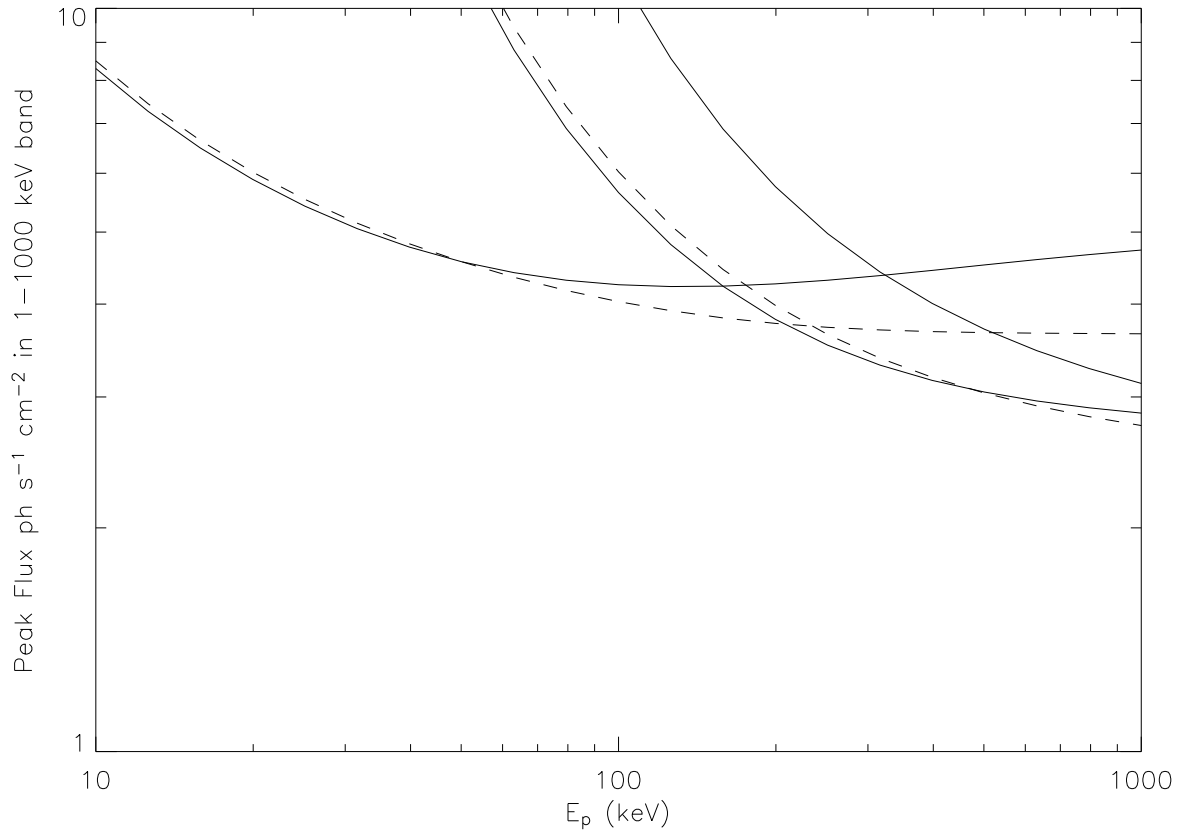Fig. 18.— Two sets of ΔE for $\alpha = 0$ and $\beta = -2$. For the first (solid curves) ΔE=5–100, 50–300, and 100–1000 keV while for the second (dashed curves) ΔE=5–1000 and 50—1000 keV. The calculation is $\sigma_0 = 5.5$ and a zenith angle of $0°$. The y-axis is the 1–1000 keV peak flux (ph s^{-1} cm^{-2}), while the x-axis is E_p in keV.

Fig. 19.— Two sets of ΔE for $\alpha = -1$ and $\beta = -25$. For the first (solid curves) ΔE=5–100, 50–300, and 100–1000 keV while for the second (dashed curves) ΔE=5–1000 and 50—1000 keV. The calculation is $\sigma_0 = 5.5$ and a zenith angle of $0°$. The y-axis is the 1–1000 keV peak flux (ph s^{-1} cm^{-2}), while the x-axis is E_p in keV.
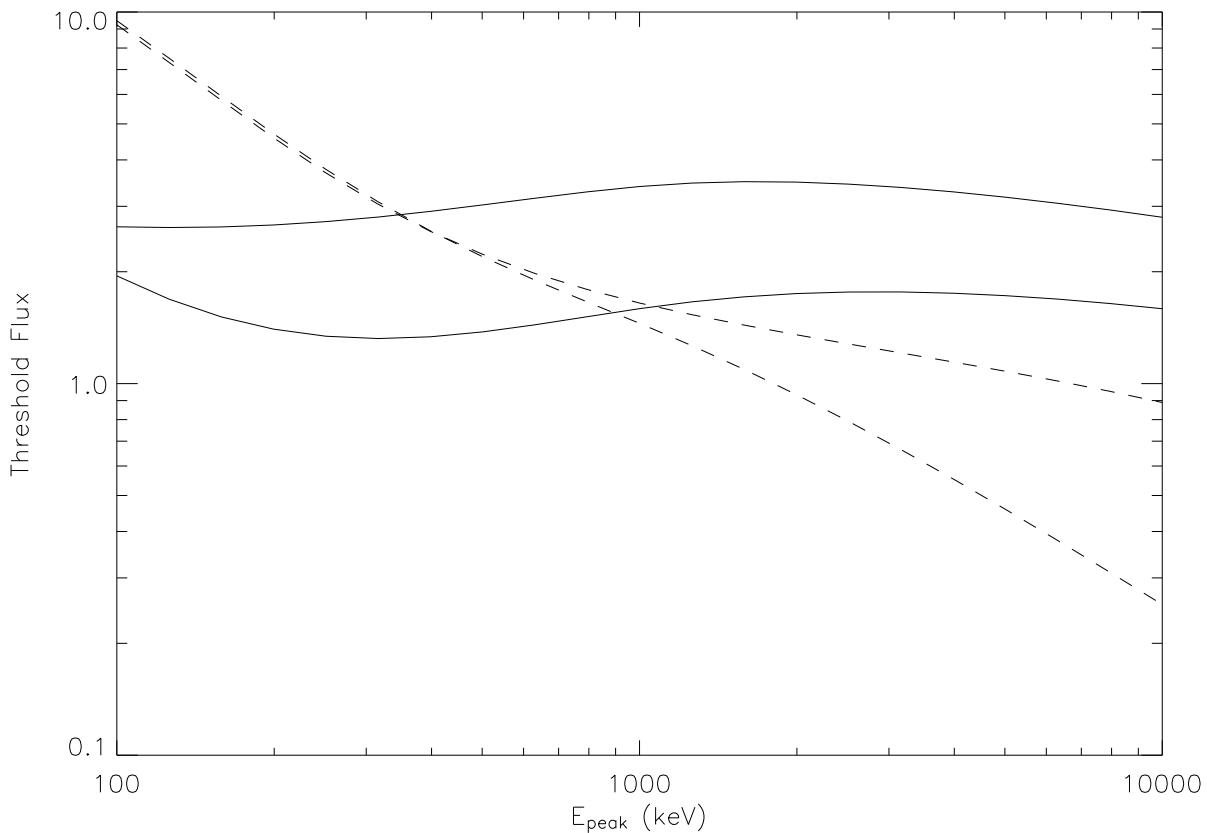
Fig. 20.— Sensitivity curves for a NaI trigger (solid) and BGO trigger (dashed) for a burst on the LAT normal with $\alpha = 0$ and $\beta = -2$. Two sets of ΔE are shown for each trigger: ΔE=5–1000 keV and 50–300 keV for NaI and ΔE=0.15–1 MeV and 0.15–30 MeV for BGO. The NaI trigger assumes two detectors triggered at $\sigma_0 = 5.5$ while the BGO trigger assumes only one detector triggered at $\sigma_0 = 8$. The y-axis is the 1–1000 keV peak flux (ph s^{-1} cm^{-2}), while the x-axis is E_p in keV.
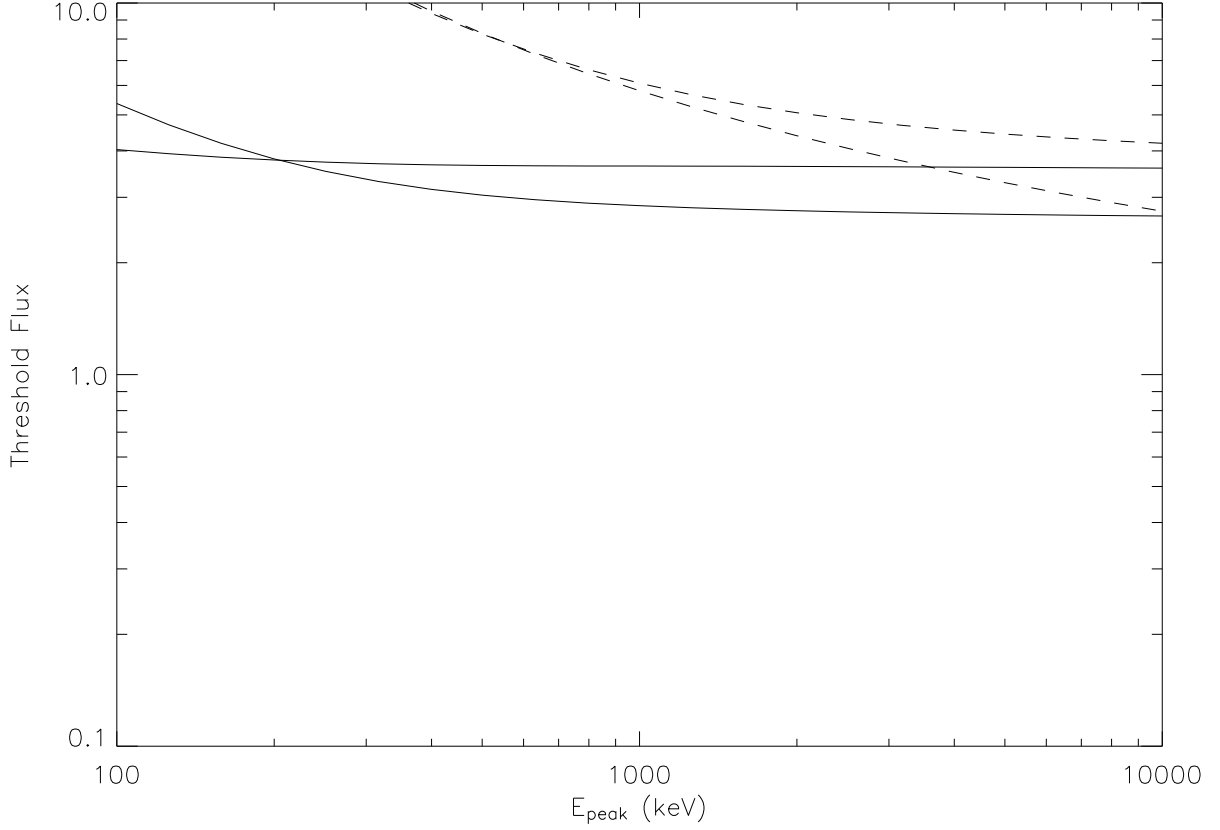
Fig. 21.— Sensitivity curves for a NaI trigger (solid) and BGO trigger (dashed) for a burst on the LAT normal with $\alpha = -1$ and $\beta = -2$. Two sets of ΔE are shown for each trigger: ΔE=5–1000 keV and 50–300 keV for NaI and ΔE=0.15–1 MeV and 0.15–30 MeV for BGO. The NaI trigger assumes two detectors triggered at $\sigma_0 = 5.5$ while the BGO trigger assumes only one detector triggered at $\sigma_0 = 8$. The y-axis is the 1–1000 keV peak flux (ph s^{-1} cm^{-2}), while the x-axis is E_p in keV.
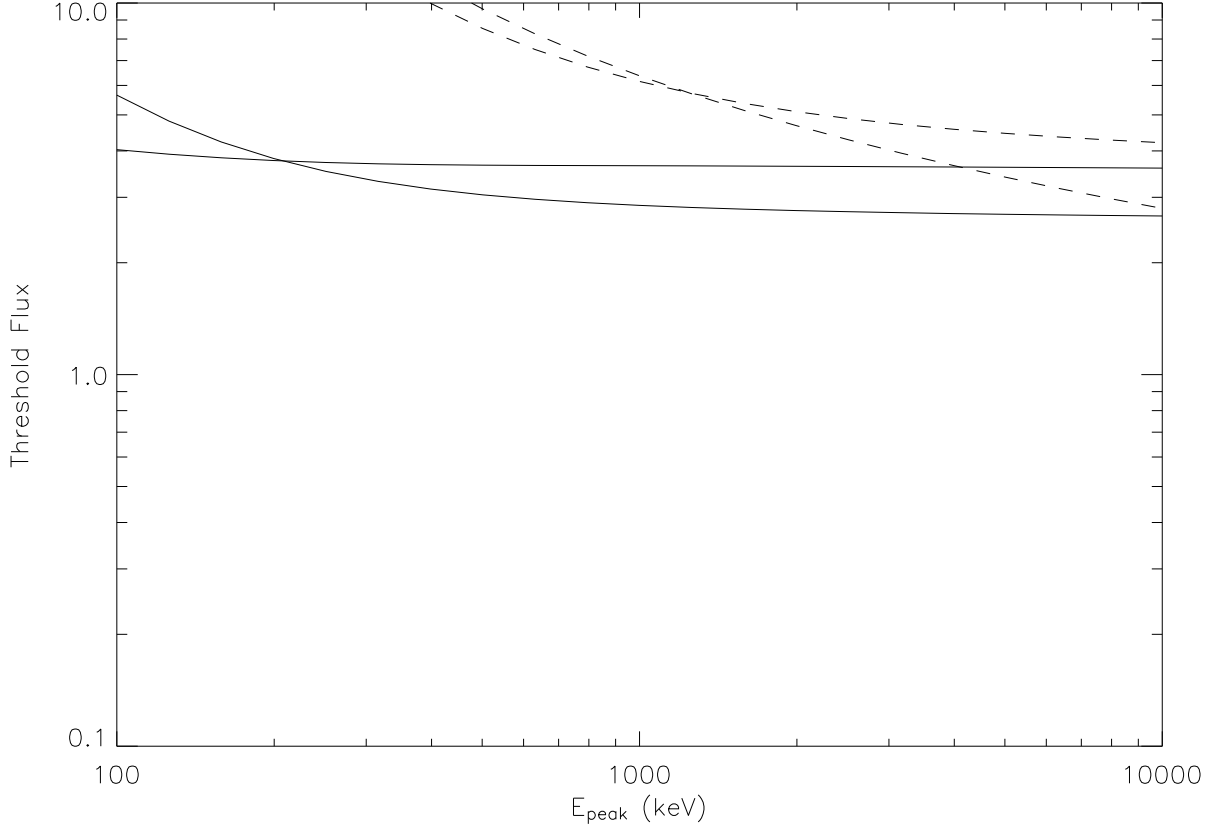
Fig. 22.— Sensitivity curves for a NaI trigger (solid) and BGO trigger (dashed) for a burst on the LAT normal with $\alpha = -1$ and $\beta = -5$. Two sets of ΔE are shown for each trigger: ΔE=5–1000 keV and 50–300 keV for NaI and ΔE=0.15–1 MeV and 0.15–30 MeV for BGO. The NaI trigger assumes two detectors triggered at $\sigma_0 = 5.5$ while the BGO trigger assumes only one detector triggered at $\sigma_0 = 8$. The y-axis is the 1–1000 keV peak flux (ph s^{-1} cm^{-2}), while the x-axis is E_p in keV.